The Journal of Chemical Physics

RESEARCH ARTICLE | OCTOBER 04 2023

Characterizing the origin band spectrum of isoquinoline with resonance enhanced multiphoton ionization and electronic structure calculations

Timothy J. Krogmeier ; Emerson S. Pappas ; Kylie A. Reardon ; Marcos R. Rivera;
Kade Head-Marsden ; Bradley F. Parsons ; Anthony W. Schlimgen

J. Chem. Phys. 159, 134305 (2023)
https://doi.org/10.1063/5.0168421

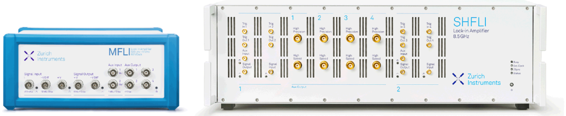

AIP Publishing

The Journal of Chemical Physics ARTICLE pubs.aip.org/aip/jcp

Characterizing the origin band spectrum of isoquinoline with resonance enhanced multiphoton ionization and electronic structure calculations

Cite as: J. Chem. Phys. **159**, 134305 (2023); doi: 10.1063/5.0168421
Submitted: 18 July 2023 • Accepted: 10 September 2023 •
Published Online: 4 October 2023

Timothy J. Krogmeier,[1] Emerson S. Pappas,[2] Kylie A. Reardon,[2] Marcos R. Rivera,[2] Kade Head-Marsden,[1] Bradley F. Parsons,[2] and Anthony W. Schlimgen[1,a)]

AFFILIATIONS

[1] Department of Chemistry, Washington University in St. Louis, St. Louis, Missouri 61630, USA
[2] Department of Chemistry and Biochemistry, Creighton University, Omaha, Nebraska 68178, USA

[a)] **Author to whom correspondence should be addressed:** santhony@wustl.edu

ABSTRACT

We report the experimental resonance enhanced multiphoton ionization spectrum of isoquinoline between 315 and 310 nm, along with correlated electronic structure calculations on the ground and excited states of this species. This spectral region spans the origin transitions to a π–π^* excited state, which previous work has suggested to be vibronically coupled with a lower lying singlet n–π^* state. Our computational results corroborate previous density functional theory calculations that predict the vertical excitation energy for the n–π^* state to be higher than the π–π^* state; however, we find an increase in the C–N–C angle brings the n–π^* state below the energy of the π–π^* state. The calculations find two out-of-plane vibrational modes of the n–π^* state, which may be brought into near resonance with the π–π^* state as the C–N–C bond angle increases. Therefore, the C–N–C bond angle may be important in activating vibronic coupling between the states. We fit the experimental rotational contour with a genetic algorithm to determine the excited state rotational constants and orientation of the transition dipole moment. The fits show a mostly in-plane polarized transition, and the projection of the transition dipole moment in the a-b plane is about 84° away from the a axis. These results are consistent with the prediction of our electronic structure calculations for the transition dipole moment of the π–π^* excited state.

I. INTRODUCTION

Organic chromophores are important molecules in nucleic acid biochemistry, in technological applications such as solar cells and organic light emitting diodes, and as species exhibiting fundamental physical phenomena such as vibrational and spin–orbit coupling in their electronic wavefunctions. These species are also highly varied and substituted, resulting in rich and informative spectra when studied in series. Isoquinoline and quinoline are the simplest azanapthalenes with the nitrogen replacing the C–H at carbon atoms 2 or 1, respectively. These molecules and their derivatives have a wide range of applications, including in pharmaceutical chemistry. For example, isoquinoline serves as the starting point in syntheses of anesthetics, antiretrovirals, and antihypertensive agents with high biological activity.[1–4] Moreover, research from the 1990s has suggested that isoquinoline derivatives may play a role in cell death from Parkinson's disease,[5,6] and more recently, isoquinoline derivatives have been investigated in therapeutic roles for the treatment of Parkinson's disease.[7–9]

With respect to quinoline, one recent study considered its use in the production of singlet oxygen,[10] which can be used in photodynamic therapeutics for cancer treatment.[11] This study considered the complexation of quinoline with O_2, followed by excitation to form singlet oxygen; however, the mechanism of formation could not be definitively identified.[10] This particular experiment on azanaphthalenes highlights the general relationship between the applications of these molecules and their fundamental underlying chemical physics. Therefore, the electronic structure of isoquinoline is important and, consequently, has been studied experimentally through gas-phase spectroscopy.[12–16] Supporting computational work has been limited, with some results for isoquinoline from density functional theory (DFT) calculations accompanying high quality UV-VUV gas phase absorption and Raman spectra.[16,17]

The low-lying excited states of aza-aromatic molecules include singlet states with either n–π^* or π–π^* electronic character, with the former being an excitation of an electron in the nitrogen lone pair into the π manifold and the latter excitation from a π orbital to a π^*.[18] The isoquinoline absorption spectrum shows a strong origin series near 312 nm that was attributed to the lowest singlet π–π^* excited state but with an irregular band spacing that could not be assigned to a regular vibrational sequence.[12] The study concluded that the observed sequence bands resulted from vibronic coupling between the π–π^* origin and two out-of-plane vibrational modes of the n–π^* state, which was modeled around 1000 cm^{-1} below the origin band. Another study then analyzed the dispersed fluorescence spectrum following the excitation of individual origin bands,[12,13] demonstrating that the spectra for individual bands were broadly similar, with small intensity variation attributed to additional coupling to a higher energy π–π^* excited state.[13] Laser excitation and dispersed fluorescence of jet cooled isoquinoline and isoquinoline clustered with methanol were also investigated.[14]

For bare isoquinoline, the spectra showed three origin band transitions in agreement with previous work, and the dispersed fluorescence spectra were essentially identical, indicating the transition strength from the π–π^* state was distributed over the origin band series. From picosecond fluorescence spectroscopy, the excited state lifetime for bare isoquinoline was also determined to be 380 ps, but the addition of methanol or water increased the lifetime, suggesting that hydrogen bonding shifts the n–π^* state in energy.[15] Isoquinoline clustered with methanol or water was also investigated using resonant ionization coupled with mass spectrometry.[19] The mass selected spectrum for isoquinoline-$(CH_3OH)_1$ and isoquinoline-$(H_2O)_1$ showed a single origin band, again suggesting the n–π^* state was shifted in energy by hydrogen bonding. The resonance enhanced multiphoton ionization (REMPI) spectrum of isoquinoline was also recorded, but the rotational contour of the spectrum was not reported.[20] The photoelectron spectrum of neutral isoquinoline was reported with ionization energies of 11.9 and 9.14 eV and showed an increasing contribution from the n–π^* excited state to higher levels of the origin band sequence.[21]

The rotational contour for isoquinoline was reported for the room temperature gas phase absorption spectrum with a resolution of 0.05 cm^{-1}.[22] At the time, the isoquinoline ground state geometry and rotational constants were not reported, so the ground state structure was estimated by merging the ground state pyridine geometry with a slightly perturbed benzene geometry. The ground state rotational constants were then estimated from the resulting isoquinoline geometry. The origin bands were fit by assuming a predominately B-type rotational contour with the higher wavenumber region of the band related to the change in the A rotational constant between the ground and excited state, while the lower wavenumber region of the band was simulated using the change in the C rotational constant between the ground and excited state.[22] A preliminary constraint of zero inertial defects was then relaxed to improve the fit. This resulted in an in-plane transition with a predominantly B-type rotational contour consistent with the initial assumption, and the transition dipole moment was oriented about 67° relative to the a-axis; however, no electronic structure results were reported for comparison.

The isoquinoline ground state rotational constants were later experimentally determined using millimeter wave spectroscopy,[23] and software using genetic algorithms[24,25] has since been developed to fit the observed rotational contours. These advances now allow for fewer assumptions to be made during analysis and thus provide for more systemic fitting of experimental data. Furthermore, the widespread use of modern molecular beam techniques allows for reduced spectral congestion in the experiment, and these improvements have been used to study the closely related indole molecule.[26,27] However, no study combining these advances has been reported for isoquinoline, which has prompted our reinvestigation for the S_2 π–π^* origin band system. We note that the S_2 state has A' symmetry electronic symmetry, and the experimental work described earlier suggests the origin band to be about 1100 cm^{-1} above the lowest singlet excited state, S_1, having n–π^* electronic character and A'' electronic symmetry. The structure for observed origin bands then results from the coupling between the S_2 origin and two nearly resonant out-of-plane a'' vibrational levels of the S_1 n–π^* state.

Despite the experimental characterization of isoquinoline, computational descriptions of its electronic structure have remained limited. Most recently, density functional theory calculations predicted that the n–π^* excited state lies 0.2 eV above the π–π^* state when considering vertical excitation energy from the ground state minimum.[16]

In order to experimentally characterize the origin band, we utilize 1 + 1′ REMPI spectroscopy with a resolution of 0.1 cm^{-1} to record the rotational contour for the origin band systems of jet cooled isoquinoline. From fits to the spectra, we extract excited state rotational constants and the orientation of the transition dipole moment to be compared with results from electronic structure theory. The observed rotational contour, along with the theoretical descriptions of the electronic states, provide important insight into the nature of the vibronic coupling in the S_1 and S_2 states. Furthermore, here we find the vertical and adiabatic excitation energies differ significantly, which is due to a difference in the equilibrium C–N–C bond angle for the two excited states. This coupling appears to be strongly geometry dependent and sensitive to a C–N–C angle change between 110 and 140°.

We use correlated active space methods, excited state coupled-cluster, and density functional theory to characterize the lowest excited states of isoquinoline, providing a more complete view of the correlation and electronic structure of this species. Here we find that the vertical excitation ordering differs depending on the electronic structure method. Our DFT calculations predict the n–π^* excited state is lower in energy, while coupled-cluster and correlated wavefunction methods predict the π–π^* state is lower. The relative energy is particularly sensitive to the C–N–C bond angle, with the n–π^* state favoring a larger bond angle than the ground and π–π^* excited states. Similar behavior has been seen in excited states in indole, pyrrole, and adenine;[26–29] in the latter case, the ground state and π–π^* state approach a conical intersection when the molecule becomes puckered. Furthermore, we compute rotational constants, vibrational frequencies, and transition dipole moments of the π–π^* state, which generally align well with experimental observations.

Specifically, we find vibrational modes of the ground, π–π^*, and n–π^* states with the appropriate symmetry and energy; the computed transition dipole moment of the π–π^* excited state is in-plane polarized; and the rotational constants agree well with fits to the experimental rotational contour.

Taken together, our experimental and computational results in Secs. III A and III B, respectively, provide significant insight into the structure of the low-lying excited states of isoquinoline. Our results provide convincing evidence for the symmetry and energy of the vibronic coupling of the S_1 and S_2 states; however, questions remain about their relative energy orderings. In Sec. IV, we suggest several experiments and possible calculations that could help clarify the remaining ambiguities in the lowest excited state spectrum of isoquinoline.

II. METHODS

A. Experimental methods

The experimental setup has been described previously,[30,31] and only relevant details are provided here. The isoquinoline (Thermo Scientific, 97%) is purified by dissolving in hexane and recrystallizing using a water-ice bath. The crystals form as clear platelets, and 10–20 mg of purified isoquinoline is placed inside the quartz sample holder of an Even-Lavie pulsed nozzle (Lamid, 150 μm orifice).[32,33] During experiments, the nozzle is heated to 80 °C and backed with a He buffer gas at a stagnation pressure of either 3 or 15 bars. The supersonic expansion is skimmed once (Beam Dynamics, 3.0 mm), and the resulting molecular beam passes along the cylindrical axis of an ion optics stack normally used for velocity map ion imaging. For REMPI experiments, the ion optic voltages were set to spatially focus ions onto a microchannel plate (MCP) detector. The resulting electron current from the MCP is then amplified using a pre-amplifier (Photek, PA200-10) and passed to a gated boxcar integrator (Stanford Research Systems, SR250). The averaged output for a particular ion mass is recorded using a USB data acquisition device.

To resonantly excite isoquinoline, we cross the molecular beam with light between 315 and 310 nm, which is generated by frequency doubling the output of an Nd:YAG pumped dye laser (Spectra-Physics Lab-190-10 Hz and Sirah Cobra Stretch, linewidth 0.10 cm^{-1} at 312 nm). The resonant excitation laser enters the interaction region unfocused with a beam diameter of 1 cm and a power density between 1×10^9 and 2×10^9 W m^{-2}. Excited state isoquinoline is photoionized through the absorption of a 266 nm photon from the fourth harmonic of an Nd:YAG laser (Amplitude SureLite EX). The 266 nm beam diameter is reduced from 1 cm to 5 mm using a telescope, which reduces the background signal from photoelectrons produced by scattered light striking the stainless steel ion optics. We control the power for both 312 and 266 nm lasers using tunable waveplates (Alphalas GmbH) and Glan-laser polarizers (Thorlabs), and timing between the lasers, gas pulse, and boxcar gate is controlled using three digital delay generators (SRS DG535 and Quantum Composers 9514+). For all experiments, the timing delay is set so the lasers are temporarily overlapped.

We calibrate the dye laser wavelength through resonant ionization of atomic iodine,[34] and the measured photon energy is corrected by -1.9 cm^{-1} with a 2σ deviation of 0.1 cm^{-1}. When accounting for the above uncertainty, the UV laser bandwidth, and the thermal drift of the dye laser, we estimate the absolute error for the experimental photon energy to be 0.5 cm^{-1}.

B. Computational methods

We used a variety of techniques to characterize the electronic structure of the ground state and the lowest π–π^* and n–π^* excited states of isoquinoline. We used the OpenMolcas[35] package to compute state-averaged (SA) Complete-Active-Space Self-Consistent-Field (CASSCF) energies and geometries with second order perturbation theory (CASPT2).[36–39] Specifically, we used SA-CASPT2 to optimize the ground, π–π^*, and n–π^* excited states with the ANO-RCC-VTZP basis.[40,41] The active space used for the calculations consisted of 12 electrons distributed among five bonding π molecular orbitals, five anti-bonding π molecular orbitals, and one non-bonding lone pair orbital, an active space denoted as $[12e, 11o]$. We do not expect significant valence-Rydberg mixing for these two excited states because there appear to be no nearby Rydberg states, and we experienced no issues with intruder states. Therefore, the active space was not extended to include any Rydberg orbitals, although this theoretically could still be a source of error.[28,42–45] The state average was computed with the ground state and either the π–π^* state or the n–π^* state, with the ground and excited states weighted equally at 50% of the state-averaged wavefunction.

We optimized the π–π^*, and n–π^* states in separate SA calculations due to the significantly different nature of their electronic states. In fact, the n–π^* state was difficult to locate in C_1 symmetry using ground state orbitals, so we initialized the calculation with the n–π^* state from a smaller CASSCF calculation of the lone pair and the 5 virtual π orbitals. The geometries were optimized using analytical gradients, and the minima were verified by computing the vibrational frequencies numerically. The n–π^* state exhibited a small imaginary frequency ($89i$ cm^{-1}), which is likely attributable to numerical noise. We utilized Cholesky density fitting and default convergence criteria for all calculations;[46] no orbitals were frozen in the CASPT2 procedure, and no point-group symmetry was used in the OpenMolcas calculations.

We also used the Orca 5 package to perform DFT, Equation-of-Motion Coupled-Cluster singles and doubles (EOM-CCSD), and N-electron-valence perturbation theory (NEVPT2) calculations for this system.[47–51] Specifically, we used the PBE, PBE0, and B3LYP density functionals to compute equilibrium geometries, vibrational frequencies, vertical and adiabatic excitation energies, and rotational constants for the two lowest excited states of isoquinoline.[52–56] We computed the excited states using TD-DFT.[57] For all DFT calculations, we used the cc-pv5z basis, while the EOM-CCSD calculations used the cc-pvtz basis.[58] The TD-DFT states were computed with four roots, while the EOM-CCSD calculations were performed with two roots. Finally, for the DFT, NEVPT2, and EOM-CCSD methods, we compute the vertical and adiabatic excitation energies for the $^1A''$ and $^1A'$ excited states using the CASPT2 equilibrium geometries. The equilibrium geometries of all states were found to be planar, even when optimized without symmetry constraints. All Orca calculations utilized the COSX density fitting procedure using the SARC/J and cc-pvnz/C auxiliary basis sets.[59,60] We found a single imaginary frequency for each of the DFT functionals when optimizing the geometry of the A' π–π^* state. This could be due to the multireference nature of this excited state, which could be challenging for TD-DFT to describe reliably.

Using Orca, we also computed state-specific (SS) CASSCF wavefunctions with NEVPT2 corrections. SS-CASSCF calculations were performed on the ground and two excited states of isoquinoline using initial guess orbitals from a single-reference Hartree–Fock calculation and converged with default convergence settings, although requiring a user-selected active space.[61] The CASSCF wavefunctions for each state were then used as input to NEVPT2 to yield the dynamic correlation correction to the energy of each state. Like in the CASPT2 calculation, no orbitals were frozen in the NEVPT2 routine; however, the CASSCF/NEVPT2 calculations utilize C_s symmetry as well as the cc-pv5z basis and accompanying auxiliary basis sets. We note that all of the active space calculations indicate that all states exhibit varying degrees of correlation, both by fractional occupations of the natural orbitals and from the configuration contributions to the wavefunction (see the supplementary material, Tables S1 and S2, respectively) The natural orbitals for each state are also shown in the supplementary material, Figs. S1–S3. The π–π^* state has major contributions from the HOMO to LUMO, and HOMO-1 to LUMO+1 transitions, while the ground state and n–π^* state have a major contributing configuration of about 82%, with many configurations making up about 1% each of the wavefunction. This indicates that a balanced treatment of static and dynamic electron correlation is likely important for consistent modeling of these three states. The HOMO-1, HOMO, LUMO, and LUMO+1 orbitals from the ground state are shown in Fig. 1.

Finally, we computed a series of constrained relaxed minima along the C–N–C bond angle coordinate. At each bond angle along the coordinate, we relax the remaining nuclei with B3LYP to generate a series of relaxed geometries between C–N–C bond angles of 110–140° in increments of one degree. At each relaxed geometry, we then compute the NEVPT2 excitation energies for the $[12e, 11o]$ active space for the $^1A''$ and $^1A'$ states. Additionally, we used TD-DFT to calculate vertical excitation energies using B3LYP, PBE, and PBE0. At each constrained geometry from the B3LYP angle scan, we used TD-DFT in single-point calculations computing four roots.

(a) LUMO+1 (b) LUMO

(c) HOMO (d) HOMO-1

FIG. 1. The frontier natural orbitals of the ground state of isoquinoline are shown. All four frontier orbitals are π-type orbitals. The complete set of natural orbitals and occupations for all states is shown in the supplementary material.

For the TD-DFT calculations, the initial guess matrix was increased in size, and the dimension of the Davidson expansion space was reduced in order to avoid negative excitation energies.

III. RESULTS

A. Experimental results

Figure 2 shows the 1 + 1′ REMPI spectrum of isoquinoline obtained with a He stagnation pressure of 3 bars, which results in less efficient cooling of isoquinoline rotational modes. Since the laser bandwidth is triple the smallest rotational constant of isoquinoline, expansion conditions that lead to inefficient rotational cooling help to spread out the rotational contour for the observed bands. Qualitatively, the bands in Fig. 2 all show a similar rotational contour with a branch structure reminiscent of a B-type transition, and the band system is labeled with the designation previously used for isoquinoline: 0^+, 0^-, and $0^=$.[13] Along with these three origin bands, we observed two weaker bands at −42 and 277 cm^{-1} relative to the 0^+ band.

Figure 3 shows the isoquinoline origin band system with a nozzle stagnation pressure of 15 bars, which should result in colder expansion conditions. Comparing Figs. 2 and 3, the branch structure in Fig. 2 has collapsed in Fig. 3, and the −42 cm^{-1} band has decreased in relative intensity. Previous work has assigned the −42 cm^{-1} band as originating from a vibrationally excited ground state, i.e., a hot band,[12] and our fits for the spectra in Figs. 2 and 3 give a rotational temperature for the 0^+ band to be about 57 and 5 K, respectively. Therefore, the relative intensity change for the −42 cm^{-1} band identifies this as a hot band. Figure 4 shows the spectra region lower in energy from the 0^+ band and was also obtained with a He stagnation pressure near 3 bars but with higher probe laser intensity. Under these conditions, we observed improved signal-to-noise but with lower spectral resolution. In Fig. 4, the −42 cm^{-1} band appears

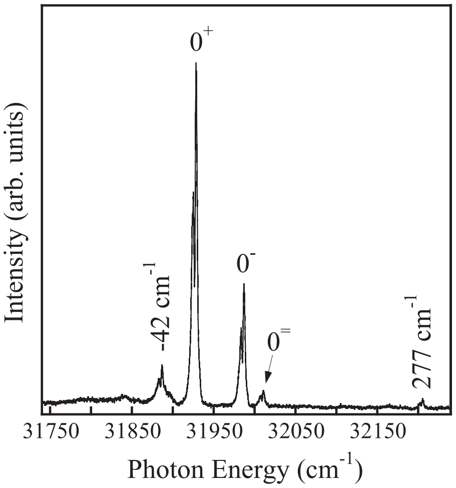

FIG. 2. 1 + 1′ isoquinoline REMPI spectrum between 315 and 310 nm with a He stagnation pressure of about 3 bars. The spectrum shows three prominent origin bands labeled as 0^+, 0^-, and $0^=$. The spectrum also shows bands at −42 and 277 cm^{-1} relative to the 0^+ band. A genetic fit to the rotational contour for the 0^+ band gives a rotational temperature of 57 K, and assignments for the transitions are discussed in the text.

TABLE I. Spectroscopic parameters obtained from fits to the experimental data. The rotational constants are given in units of cm^{-1} and (MHz), the Watson A Hamiltonian parameters in Hz, and the rotational temperature in K. The average and (maximum) deviation in the rotational constants were determined to be: A′ 16 MHz (47 MHz), B′ 10 MHz (27 MHz), and C′ 9 MHz (13 MHz). The average and (maximum) deviation in the rotational temperature were 2 K (5 K). The average and (maximum) deviation in Θ were 13°(19°), and for Φ, it was 4°(10°).

	0^+	0^-	$0^=$	42 cm^{-1} band
A′ (cm^{-1})	0.1049 (3143.9)	0.1050 (3148.5)	0.1051 (3150.4)	0.1051 (3151.1)
B′ (cm^{-1})	0.0417 (1249.8)	0.0417 (1250.6)	0.0414 (1240.4)	0.0417 (1250.9)
C′ (cm^{-1})	0.0295 (885.3)	0.0295 (883.8)	0.0295 (885.6)	0.0296 (887.1)
Δ_J (Hz)	54.3	159.6	226.1	141.1
Δ_{JK} (Hz)	113.3	110.6	114.0	347.1
Δ_K (Hz)	366.3	244.2	169.5	205.2
δ_J (Hz)	5.98	27.4	39.1	28.2
δ_K (Hz)	65.4	66.7	66.7	65.5
μ_a^2:μ_b^2:μ_c^2	0.005:0.929:0.066	0.005:0.918:0.077	0.004:0.891:0.105	0.002:0.910:0.088
Temperature (K)	57.3	59.5	61.6	65.3
Θ (deg)	86	86	86	87
Φ (deg)	75	74	71	73

just to the red of the origin onset, and several additional hot bands are also observed at −84, −113, −132, and −210 cm^{-1}.

Figure 5 shows an expanded view of the observed rotational contour for the 0^+ band. We fit the observed contour using the genetic fitting algorithm included with the JB64 program.[24,25] For the fit, the experimental ground state constants and Watson A Hamiltonian parameters were taken from Kisiel *et al.*'s rotational spectrum.[23] The fit then optimized the excited state rotational constants, which we denote as A′, B′, and C′, the Watson A parameters, the origin for each band, the transition dipole moment orientation, and a single rotational temperature. The red curve in Fig. 5 shows the fit to the experimental data for the 0^+ band, black points, using constants taken as the average from several genetic fits. Fits to the 0^-, $0^=$, and −42 cm^{-1} can be found in Figs. S4–S6 of the supplementary material. The hot bands shown in Fig. 4 were not fit due to lower experimental resolution, and band origins were instead estimated from the band center. In Table I, we summarize the average excited state rotational constants, temperature, and normalized weighting for the transition dipole moment along the a, b, and c inertial axes. For all bands in Table II, we also give the excitation energy and location relative to the 0^+ origin band.

Finally, from the normalized weights of the transition dipole moment, we determined the angle with respect to the b-rotational axis as $\tan\Theta = \mu_b/\mu_a$. Likewise, the angle between the transition dipole moment and the c-axis, Φ, is given by $\cos\Phi = \mu_c/\mu$. These angles were calculated using the experimental weights, and the results are included in Table I.

B. Computational results

We optimized the geometries of the ground and first two excited states using SA-CASPT2/ANO-RCC-VTZP and DFT/cc-pv5z levels of theory, using PBE, PBE0, and B3LYP density functionals. All four methods resulted in similar geometries for all states. The root-mean-square-difference of the DFT optimized geometries compared to the CASPT2 geometries was 0.01–0.02 Å for all three states (see the supplementary material, Table S3). Noting that all three states are found to be planar, the most important remaining geometric parameter is the C–N–C bond angle. Table III shows the rotational constants and the C–N–C bond angles for the three states for each of the four geometry optimization techniques. The rotational constants are all very similar, and all methods distinguish different bond angles for each of the states. In particular, the ground state geometry has a C–N–C angle of about 117°, the π–π^* excited state angle is about 115°, and the n–π^* excited state has a much larger angle, around 131° or larger. The rotational constants agree well with the constants obtained from the fit of experimental data in Table I.

We also obtained the harmonic vibrational frequencies from the DFT and SA-CASPT2 calculations. With the exception of the ground state DFT calculations, all frequencies were computed via numerical differentiation. We list the notable vibrational frequencies for the ground and lowest excited states in Table IV. There was a small imaginary frequency (about 89i cm^{-1}) for the n–π^* geometry

TABLE II. Band positions from the observed spectra in Figs. 2 and 4. All energies are in units of (cm^{-1}).

Label	Energy (cm^{-1})	Relative to 0^+ (cm^{-1})	Reference 12 (cm^{-1})
…	32 202	277	32 203
$0^=$	32 007.5	82.4	32 008.1
0^-	31 983.5	58.4	31 982.6
0^+	31 925.1	0	31 924.9
…	31 883	−42	31 885.3
…	31 841	−84	31 840.6
…	31 812	−113	…
…	31 793	−132	31 797.0
…	31 715	−210	…

TABLE III. Rotational constants (cm^{-1}) and C–N–C bond angles (°) for geometries of the ground state, π–π^*, and n–π^* excited states optimized with SA-CASPT2 and DFT, with PBE, PBE0, and B3LYP functionals.

State	Method	A (cm^{-1})	B (cm^{-1})	C (cm^{-1})	∠ C–N–C (°)
$^1A''$ ground	SA-CASPT2	0.1087	0.0422	0.0304	117.1
	PBE	0.1064	0.0411	0.0297	117.3
	PBE0	0.1080	0.0417	0.0301	117.5
	B3LYP	0.1074	0.0415	0.0299	117.6
$^1A'$ π–π^*	SA-CASPT2	0.1066	0.0413	0.0298	115.5
	PBE	0.1071	0.0400	0.0291	114.7
	PBE0	0.1085	0.0407	0.0296	114.9
	B3LYP	0.1078	0.0406	0.0295	115.1
$^1A''$ n–π^*	SA-CASPT2	0.1078	0.0422	0.0303	134.8
	PBE	0.1059	0.0411	0.0296	131.4
	PBE0	0.1072	0.0418	0.0301	132.6
	B3LYP	0.1067	0.0415	0.0299	132.2

computed from SA-CASPT2, but this may be the result of numerical noise in the calculation of the frequencies. The ground state lowest bending frequencies all give reasonable agreement with the experiment (176 or 182 cm^{-1}),[12,62] with the SA-CASPT2 and B3LYP results giving the best agreement. The SA-CASPT2 π–π^* lowest vibrational frequency is about 139 cm^{-1} and is an out-of-plane bend of a'' vibrational symmetry. This is in excellent agreement with the experimentally observed difference between the lowest vibrational level of the ground state and π–π^* states, with the experiment predicting a 42 cm^{-1} difference[12] and SA-CASPT2 predicting a 33 cm^{-1} difference between the lowest a'' mode of the ground and excited states. The experimental results suggest the n–π^* state couples to the π–π^* through two out-of-plane vibrational modes with frequencies near about 1100 cm^{-1}. Therefore, we report two a'' out-of-plane vibrational frequencies for the n–π^* state from each method. All of the methods find vibrational frequencies of the appropriate symmetry; however, in all cases, the predicted frequencies are around 900–1000 cm^{-1}. A complete listing of computed vibrational frequencies is included in Tables S4–S6 in the supplementary material, and we discuss vibrational band assignments in Sec. IV.

Choosing the SA-CASPT2 geometry as the reference geometry, we compute the vertical and adiabatic excitation energies for the $^1A'$ and $^1A''$ excited states. Table V shows the vertical excitation energies using several different methods with the CASPT2 geometries. The NEVPT2 and EOM-CCSD results all indicate that the π–π^* excited state is lower in energy than the n–π^* state at vertical excitation. The density functional theory results, on the other hand, show the opposite. At this C–N–C bond angle, about 117°, the DFT results predict the n–π^* state will be lower in energy than the π–π^* state.

When comparing the adiabatic excitation energies, however, all of the methods give the same ordering of the low-lying spectrum, as seen in Table V. Namely, the n–π^* state is consistently the lower energy excited state. The range of the excitation energies is rather large from 3 to 4 eV, while for the π–π^* state, the range is only 4–4.5 eV. We also expect the n–π^* state to exhibit the largest change from the vertical to adiabatic energy due to the significant change in the bond angle, from ∼117° to ∼130°, between the vertical and

TABLE IV. Notable vibrational frequencies (cm^{-1}) for the ground state and first two excited states of isoquinoline. The ground and π–π^* state lowest frequencies are listed, along with the n–π^* modes that may allow for vibronic coupling of the π–π^* and n–π^* states.

	Vibrational frequencies (cm^{-1})				
State	SA-CASPT2	PBE	PBE0	B3LYP	Symmetry
Ground	172	164	156	173	a''
π–π^*	139	145	149	181	a''
n–π^*	916	913	939	930	a''
n–π^*	955	1013	1002	999	a''

TABLE V. Vertical (above) and adiabatic (below) excitation energies (eV) for NEVPT2, DFT, and EOM-CCSD from the CASPT2 ground state equilibrium geometry. A negative Δ indicates that the $^1A'$ state is lower in energy than the $^1A''$ state.

	Vertical excitation energy (eV)		
Method	$^1A'$ $(\pi-\pi^*)$	$^1A''$ $(n-\pi^*)$	Δ
NEVPT2	4.54	4.82	−0.28
EOM-CCSD	4.54	4.92	−0.38
PBE	4.25	3.56	0.69
PBE0	4.57	4.42	0.15
B3LYP	4.48	4.32	0.16
	Adiabatic excitation energy (eV)		
Method	$^1A'$ $(\pi-\pi^*)$	$^1A''$ $(n-\pi^*)$	Δ
NEVPT2	4.38	4.12	0.26
EOM-CCSD	4.07	3.54	0.53
PBE	4.01	3.05	0.96
PBE0	4.48	3.85	0.63
B3LYP	4.28	3.77	0.51

adiabatic excitations, respectively. The π–π^* equilibrium bond angle is only about 2° different than the ground state, and the similarity between the vertical and adiabatic excitation energies reflects that.

These comparisons suggest further investigation into the geometric dependence of the excitation energies. Figure 6 shows the vertical excitation energies for NEVPT2 [Fig. 6(a)], PBE0 [Fig. 6(b)], and PBE [Fig. 6(c)] along a reaction coordinate θ. In this case, θ is the C–N–C bond angle, and each point represents a constrained optimization of a planar geometry with the given angle. The NEVPT2 geometries are taken from the B3LYP constrained optimizations.

We emphasize that this reaction coordinate is not meant to represent the vibronic coupling between the π–π^* and n–π^* states. The vibronic coupling occurs through an antisymmetric out-of-plane bending mode, whereas the reaction coordinate in Fig. 6 maintains a planar geometry throughout. Instead, this figure shows the change from the vertical to the adiabatic excitation energy as a function of the C–N–C bond angle. Indeed, along these slices of the hypersurfaces, we find that the crossing point of the excited states is strongly method dependent. The NEVPT2 results show the crossing at about 122°, the PBE0 is about 115°, and the PBE does not predict a crossing above 110°. Additional TD-DFT data using the B3LYP functional predicted the same crossing point angle as PBE0 and can be found in Fig. S6 in the supplementary material.

TABLE VI. Oscillator strength in arbitrary units for the π–π^* and n–π^* transitions, and the transition dipole moment angle (TDMA), Θ, in degrees in the *a*-*b* rotational plane of the molecule for the π–π^* state, relative to the *a* rotational axis. Computed at the SA-CASPT2 ground state equilibrium geometry for various levels of theory.

Method	State	Osc. Strength (a.u.)	TDMA (deg)
NEVPT2	π–π^*	0.0087	76.5
	n–π^*	0.0052	
EOM-CCSD	π–π^*	0.0188	76.0
	n–π^*	0.0021	
PBE	π–π^*	0.0489	85.8
	n–π^*	0.0005	
PBE0	π–π^*	0.0594	83.5
	n–π^*	0.0015	
B3LYP	π–π^*	0.0578	83.9
	n–π^*	0.0014	

Table VI shows oscillator strengths for the π–π^* and n–π^* transitions, as well as the transition dipole moment angle (TDMA) for the former (Θ). The oscillator strengths predicted by the various methods for the two excited states are generally consistent. The relatively low intensity of the n–π^* transition is significantly weaker than the π–π^* transition in the experiment, and the electronic structure calculations are consistent with this observation.[20] The calculations all find the oscillator strength of the π–π^* transition is significantly stronger than the n–π^*; in most cases, the π–π^* transition is an order of magnitude stronger. The exception is the NEVPT2 result, which predicts a difference between the oscillator strengths by about a factor of two. Furthermore, given the similarity between the ground state and π–π^* equilibrium geometries, we expect a much stronger Franck–Condon overlap compared to the overlap between the ground and n–π^* states with their significantly different C–N–C bond angles. The relative oscillator strength and likely Franck–Condon overlap are consistent with the relative intensities of these two states seen in the experiment. In contrast, there is a difference between the transition dipole moment angles when comparing the DFT results to the CCSD and NEVPT2 results. Namely, the DFT calculations all predict a transition dipole moment angle around 83–85°, while CCSD and NEVPT2 suggest an angle of about 76°. Interestingly, our experimental data indicates the transition dipole moment angle is about 84°, while previous work suggested an angle of 67°.[22] We visualize the transition dipole moment angle, Θ, in Fig. 7, which shows isoquinoline on the *a*-*b* rotational axis.

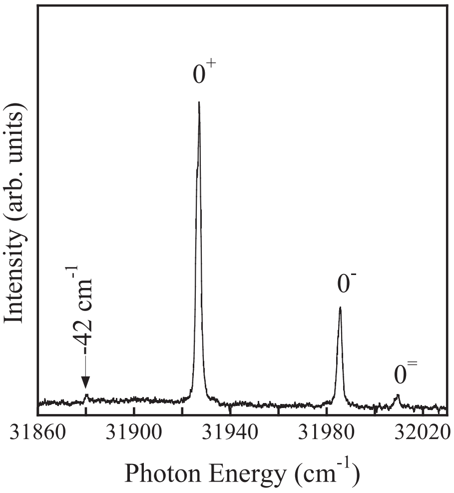

FIG. 3. 1 + 1′ isoquinoline REMPI spectrum near between 314 and 312 nm obtained a He stagnation pressure of 15 bars. The genetic fit to the rotational contour for the 0^+ band gives a rotational temperature of about 5 K, and the intensity of the −42 cm^{-1} band has decreased confirming this to be a hot band.

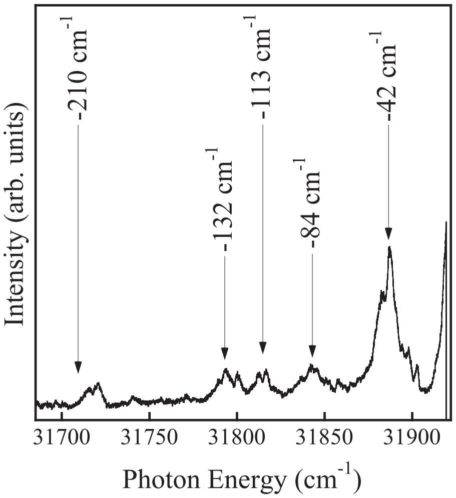

FIG. 4. 1 + 1′ isoquinoline REMPI spectrum below the 0^+ band with a He stagnation pressure of 3 bars. The indicated bands correspond to hot band transitions from excited vibrational levels of the ground electronic state.

IV. DISCUSSION AND CONCLUSIONS

Others have reported the experimental values for the ground state rotational constants to be 0.106 707, 0.041 293, and 0.029 779 cm^{-1}.[23] Overall, the experimental ground state values are in best agreement with our PBE results given in Table III.[23] Previous experimental results report rotational constants of the 0^+ band as 0.106 84, 0.041 60, and 0.030 01 cm^{-1}, which were determined as differences from estimates of the ground state rotational constants.[22] These are in reasonable agreement with our experimental values in Table I, with the largest deviation in the A' rotational constant. For the ${}^1A'$ π–π^* state, the calculated rotational constants are generally larger than the previous experimental results as well as those from our fits shown in Table I, but overall, the SA-CASPT2 results give the best agreement with the experimental numbers. Interestingly, the PBE results for the ${}^1A''$ n–π^* state give the closest agreement with our experiment; however, this is coincidental since excitation to the n–π^* excited state would result in an out-of-plane polarized transition dipole moment giving a C-type rotational contour, which is inconsistent with the experimental observation.

We next consider assignments for the non-origin bands in the spectra shown in Figs. 2 and 4. We first note that for a molecule with C_s symmetry, such as isoquinoline, the totally symmetric irreducible representation is A'. For a dipole allowed transition, the direct product of the ground vibronic state $(\Gamma_{gs,el} \otimes \Gamma_{gs,vib})$, the transition dipole moment (Γ_μ), and the excited vibronic state $(\Gamma_{es,el} \otimes \Gamma_{es,vib})$ must contain the A' irreducible representation, i.e., $\Gamma_{es,el} \otimes \Gamma_{es,vib} \otimes \Gamma_\mu \otimes \Gamma_{gs,el} \otimes \Gamma_{gs,vib} \supseteq A'$. Both the ground and S_2 π–π^* excited states have A' electronic symmetry, and so for transition to be allowed, the vibrational symmetry of the ground and excited states must be identical. Figure 2 shows a band 277 cm^{-1} above the 0^+ origin that was also observed in the gas phase absorption spectrum.[12] This band was assigned as a transition from the ground state to two quanta of the lowest out-of-plane (a'') vibrational levels of the S_2 π–π^* excited state, which is allowed with an overall A' symmetry. Our SA-CASPT2 calculations show the lowest energy vibrational mode of the π–π^* excited state corresponds with an out-of-plane a'' symmetry vibration having a frequency of 139 cm^{-1}, which is in good agreement with the earlier estimates and with our current experiment.[12] We also note that the band profile for the +277 cm^{-1} band, which is shown in Fig. S7 of the supplementary material, has a predominantly B-type rotation contour consistent with expectations for the π–π^* excited state.

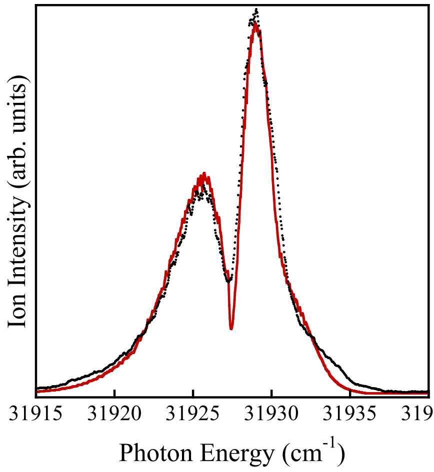

FIG. 5. Rotational contour from the 0^+ band shown in Fig. 5. The red curve was generated using the average results of several genetic fits to the observed spectrum.

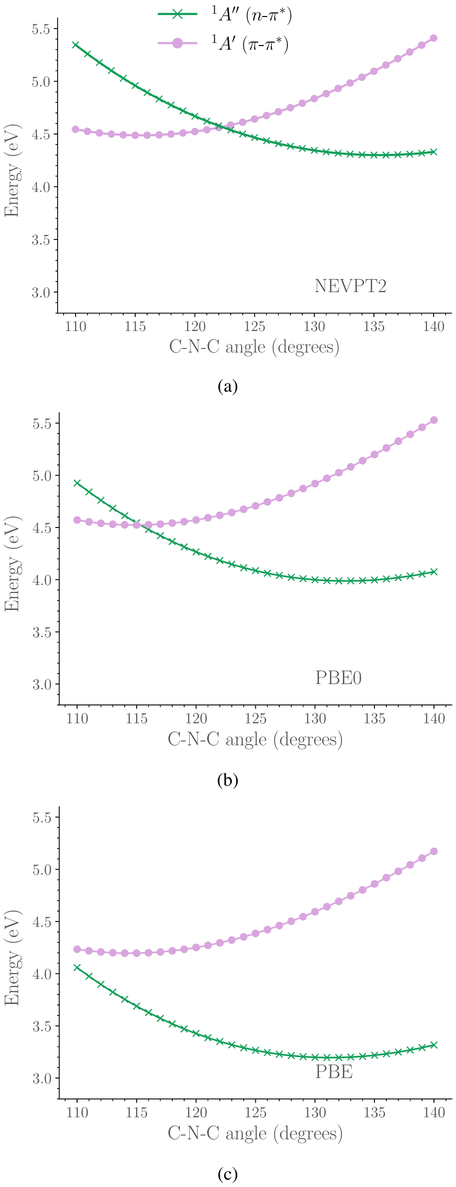

FIG. 6. The excited state energy is shown as a function of the C–N–C angle for three different levels of theory: NEVPT2 (a), PBE0 (b), and PBE (c). The data for B3LYP is shown in the supplementary material.

Figure 2 also shows a band at −42 cm^{-1}, and the intensity is reduced in Fig. 3. Based on fits to the data, the former spectrum has a rotational temperature near 60 K, while the latter has a rotational temperature of about 5 K. As discussed earlier, the reduced intensity of the −42 cm^{-1} band in Fig. 3 identifies this as a hot band. The absorption spectrum showed sequence bands with a spacing of about 40 cm^{-1} that were attributed to hot band transitions originating from a 175.5 cm^{-1} ground state vibration and terminating in the 135.5 cm^{-1} π–π^* excited state mode.[12] The isoquinoline Raman spectra show the lowest vibrational frequency at 182 cm^{-1} in agreement with the above-mentioned estimate,[12,62] and our SA-CASPT2 calculations gave the lowest ground state vibrational frequency as 172 cm^{-1} and the lowest vibrational frequency of the π–π^* excited state as 139 cm^{-1}, respectively, and both frequencies correspond with a'' out-of-plane modes. A transition from the lowest a'' ground state vibration to the lowest a'' vibration of the π–π^* excited state would be symmetry allowed, occur near −40 cm^{-1}, and show a B-type rotational contour. This is consistent with the −42 cm^{-1} band having a transition dipole moment with $\mu_b^2 = 0.910$ (Table I). As shown in Table IV, the SA-CASPT2 frequencies align with the experiment and indicate a band may be observed at −33 cm^{-1} relative to the 0^+ origin, from the difference between the lowest frequencies of the ground (172 cm^{-1}) and excited states (139 cm^{-1}). Therefore, the −42 cm^{-1} band can be assigned as a difference transition between the excited vibrational levels of both electronic states. Figure S8 of the supplementary material depicts this difference transition. Furthermore, the observed bands at −84 cm^{-1} and −132 cm^{-1} in Fig. 4 may then be assigned as involving either two or three quanta of this difference transition, respectively.

The hot band at −210 cm^{-1} was assigned as originating from an a'' vibration, which has an observed frequency of 201 cm^{-1} in the Raman spectrum.[12,62] The SA-CASPT2 calculations give the second lowest ground state vibrational frequency as 193 cm^{-1}, corresponding to an a'' mode. Based on symmetry arguments, such a transition must use an out-of-plane transition dipole, which could only result from an n–π^* excited state character. This would imply a C-type rotational contour, although the signal-to-noise ratio in our data is not sufficient to properly assess this. Alternatively, the observed transitions at −201 and −113 cm^{-1} may also result from relatively weak difference transitions like the −42 cm^{-1} sequence discussed earlier. Our SA-CASPT2 vibrational frequency calculation, Tables S4–S6 in the supplementary material, finds an a'' mode of the ground state at 472 cm^{-1} and an a'' mode of the π–π^* excited state at 264 cm^{-1}. A transition between these states would be shifted by −208 cm^{-1}, which could also account for the −210 cm^{-1} band. Likewise, a transition between the 392 cm^{-1} a'' ground state vibrational mode and the 264 cm^{-1} a'' excited state vibration mode would appear at −128 cm^{-1}, and with frequency scaling, this could potentially account for the −113 cm^{-1} mode. In our 60 K expansion, we expect these higher vibrational modes to have a reduced population relative to the 175 cm^{-1} mode, which could also account for the reduced intensity of these modes relative to the −42 cm^{-1} band.

The computational results give reasonably good agreement with the vibrational frequencies observed in the experimental spectra; however, ambiguities remain in the calculations, in particular in the energetic ordering of the states as well as the transition dipole moment angle. The EOM-CCSD and NEVPT2 calculations suggest the transition dipole moment to be in the molecular plane with an angle of about 76° relative to the a rotational axis, while the DFT results indicate the angle is closer to 84°. The observed rotational contour in Fig. 5 is consistent with a predominantly B-type transition dipole moment, and our experimental value for the in-plane orientation of the transition dipole moment agrees fairly well with the DFT results. Interestingly, the previous result was more in line with the CCSD and NEVPT2 calculations.[22] While the earlier result was recorded at a higher resolution than our work, 0.05 vs 0.1 cm^{-1}, the previous data were fit using estimated ground state rotational constants and restricting the transition dipole moment to be in-plane polarized. In comparison, our data were fit using experimental values for the ground state rotational constant and a genetic algorithm as a global optimizer with no in-plane restriction. We note that the genetic fit also gave a small contribution from an out-of-plane C-type transition dipole moment, but this weak out-of-plane character would be underlying the rotational contour towards the center of the band. The magnitude of this out-of-plane character must be taken with caution, and confirmation would require a high resolution spectrum that ideally resolves individual rotational transitions. A definitive determination of the transition dipole moment awaits such an experiment.

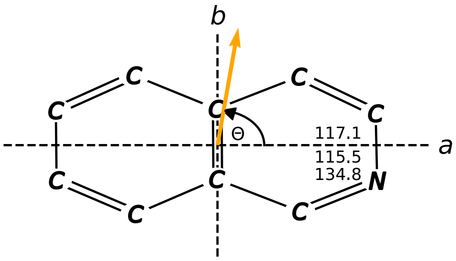

FIG. 7. The geometry of isoquinoline is shown overlayed with the a and b inertial axes. The ground state, π–π^*, and n–π^* C–N–C angles (θ) are inset from top to bottom. Additionally, the π–π^* state transition dipole moment angle, (Θ), is shown at 80° relative to the a inertial axis by the vector from the origin.

A definitive assignment of the excited state ordering may be elusive. While the experiment consistently places the π–π^* origin band just below 4 eV, all of our calculations predict the vertical excitation energy of that state to be about 4.2–4.5 eV, as shown in Table V. The DFT calculations indicate that the n–π^* state is the lowest energy state at vertical excitation, but the EOM-CCSD and NEVPT2 suggest the lower state is the π–π^*. The adiabatic energy shown in Table V is more consistent with the n–π^* state, which is lower in energy for all methods. We note that the NEVPT2, PBE0, and B3LYP π–π^* adiabatic excitation energies are still significantly above the experimental observation of about 4 eV.

A similar situation occurs in the related system indole. In that case, the L_a and L_b π–π^* excited states also approach a conical intersection along an in-plane reaction coordinate.[26,27] Depending on the electronic structure method, the conical intersection occurs at a different point along the reaction coordinate, similar to the state crossing we observe between the π–π^* and n–π^* excited states of isoquinoline. Furthermore, the relative energy of the two states is also method dependent in both the cases of indole and isoquinoline. An important difference between the indole and isoquinoline cases is the in-plane vs out-of-plane vibrations (respectively) that account for the vibronic coupling. In the current work, we have emphasized the role of the C–N–C bond angle in the excited state energies, but a more complete understanding of the vibronic coupling needs to include the out-of-plane motion of the relevant states of isoquinoline.

Resolving these discrepancies may require significant computational and experimental effort. For example, higher quality CC calculations may give more reliable energies and transition dipoles. Caution may be required, as all three of the states studied here exhibit varying degrees of electron correlation, which can be challenging for CC-based approaches to describe in a balanced fashion. In particular, we note that the $^1A'$ π–π^* excited state is predominately made up of two configurations, the HOMO to LUMO excitation and the HOMO-1 to LUMO+1 excitation, in proportions of 45 and 26%, respectively (see Table S2 in the supplementary material). All three states exhibit fractional occupations in the π manifold, which is an indicator of strong correlation as well (see Table S1 in the supplementary material). Although the ground state and n–π^* excited states are made up of a single dominant configuration (about 82%), they have many configurations contributing about 1% to the wavefunction, which can necessitate accurate treatment of dynamic correlation.

A more complete study of the potential surface, including along the out-of-plane bend, would likely yield insight into the location of conical intersections on the surface, as seen in other studies.[29,63,64] Finally, the calculation of the vibronic coupling to simulate the experimental spectrum may provide evidence to determine if the DFT or the EOM-CCSD and NEVPT2 state ordering is more accurate. We also note, however, that computational resolution in excitation energies for molecular excited states may be limited in this context. For example, EOM-CCSD and NEVPT2 excited state calculations have shown errors up to about 0.2 eV for systems of similar complexity.[45,65,66]

Experimentally, reducing the laser bandwidth below 0.1 cm^{-1} is required to obtain better measurements for the rotational constants and orientation of the transition dipole moment. Extending such experiments to record the rotational contour for the n–π^* origin, thought to be 1100 cm^{-1} below the 0^+ band, would allow for definitive assignment for the adiabatic transition to the lower state. Furthermore, mass resolved REMPI experiments measuring the rotational contour for transitions of isoquinoline clustered with hydrogen bonding or a more weakly interacting solvent may prove insightful, particularly with the latter showing smaller shifts of the n–π^* origin. Finally, the anion photoelectron spectrum of isoquinoline may also assist in confirming the location of the singlet and triplet states.

In summary, we have for the first time demonstrated a pronounced C–N–C angle dependence on the excited state ordering using correlated electronic structure methods, a geometry dependence that is likely to be important in the activation of the vibronic coupling between the n–π^* and π–π^* states. Taken in conjunction with the excited state vibrational levels from the electronic structure calculations, this begins to explain the origin for the unusual band spacing for the S_2 origin of isoquinoline. We have used a genetic algorithm to fit the experimental rotational band contour from the REMPI spectrum of the origin bands and determined the excited state rotational constants and orientation of the transition dipole moment with respect to the a-axis. These results are consistent with theoretical predictions. Moreover, we have shown the theoretical vibrational frequencies are consistent with the observed hot bands from the experiment and with the observed band 277 cm^{-1} above the origin transition. These results provide deeper knowledge about isoquinoline and can inform future experiments, as described earlier.

SUPPLEMENTARY MATERIAL

See the supplementary material for visualization of molecular orbitals, orbital occupations, and complete lists of vibrational frequencies, along with additional experimental spectra and computational data.

ACKNOWLEDGMENTS

The experiments in this work were supported by the National Science Foundation under Grant No. CHE-2150871. We would like to acknowledge Dr. David Plusquellic for providing the JB64 program used to fit the experimental rotational contours.

AUTHOR DECLARATIONS

Conflict of Interest

The authors have no conflicts to disclose.

Author Contributions

Timothy J. Krogmeier: Data curation (equal); Writing – original draft (equal). **Emerson S. Pappas**: Data curation (equal). **Kylie A. Reardon**: Data curation (equal). **Marcos R. Rivera**: Data curation (equal). **Kade Head-Marsden**: Conceptualization (equal); Supervision (equal); Writing – original draft (equal). **Bradley F. Parsons**: Conceptualization (equal); Data curation (equal); Writing – original draft (equal). **Anthony W. Schlimgen**: Conceptualization (equal); Data curation (equal); Writing – original draft (equal).

DATA AVAILABILITY

The data that support the findings of this study are available from the corresponding author upon reasonable request.

REFERENCES

[1] Z.-X. Qing, P. Yang, Q. Tang, P. Cheng, X.-B. Liu, Y.-j. Zheng, Y.-S. Liu, and J.-G. Zeng, "Isoquinoline alkaloids and their antiviral, antibacterial, and antifungal activities and structure-activity relationship," Curr. Org. Chem. **21**, 1920–1934 (2017).

[2] D. Taniyama, M. Hasegawa, and K. Tomioka, "A facile and efficient asymmetric synthesis of (+)-salsolidine," Tetrahedron Lett. **41**, 5533–5536 (2000).

[3] E. L. Anderson, J. W. Wilson, and G. E. Ullyot, "Isoquinoline derivatives as local anesthetics," J. Am. Pharm. Assoc., Sci. Ed. **41**, 643–650 (1952).

[4] E. J. Fellows and E. Macko, "The topical anesthetic activity of an isoquinoline compound," J. Pharmacol. Exp. Ther. **103**, 306–309 (1951).

[5] T. Nagatsu, "Isoquinoline neurotoxins in the brain and Parkinson's disease," Neurosci. Res. **29**, 99–111 (1997).

[6] K. S. McNaught, P.-A. Carrupt, C. Altomare, S. Cellamare, A. Carotti, B. Testa, P. Jenner, and C. Marsden, "Isoquinoline derivatives as endogenous neurotoxins in the aetiology of Parkinson's disease," Biochem. Pharmacol. **56**, 921–933 (1998).

[7] R.-H. Fu, Y.-C. Wang, C.-S. Chen, R.-T. Tsai, S.-P. Liu, W.-L. Chang, H.-L. Lin, C.-H. Lu, J.-R. Wei, Z.-W. Wang, W.-C. Shyu, and S.-Z. Lin, "Acetylcorynoline

attenuates dopaminergic neuron degeneration and α-synuclein aggregation in animal models of Parkinson's disease," Neuropharmacology **82**, 108–120 (2014).

[8] K. Yang, G. Jin, and J. Wu, "The neuropharmacology of (-)-stepholidine and its potential applications," Curr. Neuropharmacol. **5**, 289–294 (2007).

[9] E. Plazas, M. C. Avila M, D. R. Muñoz, and L. E. S. Cuca, "Natural isoquinoline alkaloids: Pharmacological features and multi-target potential for complex diseases," Pharmacol. Res. **177**, 106126 (2022).

[10] B. F. Parsons, M. R. Rivera, M. A. Freitag, K. A. Reardon, E. S. Pappas, and J. T. Rausch, "Singlet O_2 from ultraviolet excitation of the quinoline-O_2 complex," J. Phys. Chem. A **127**, 4957–4963 (2023).

[11] P. S. Maharjan and H. K. Bhattarai, "Singlet oxygen, photodynamic therapy, and mechanisms of cancer cell death," J. Oncol. **2022**, 7211485.

[12] G. Fischer and R. Naaman, "Near Resonance vibronic coupling. Isoquinoline," Chem. Phys. **12**, 367–379 (1976).

[13] G. Fischer and A. E. Knight, "Narrow band laser excited fluorescence as a probe of the near-resonance vibronic coupling in isoquinoline vapor," Chem. Phys. **17**, 327–342 (1976).

[14] P. M. Felker and A. H. Zewail, "Jet spectroscopy of isoquinoline," Chem. Phys. Lett. **94**, 448–453 (1983).

[15] P. M. Felker and A. H. Zewail, "Stepwise solvation of molecules as studies by picosecond-jet spectroscopy: Dynamics and spectra," Chem. Phys. Lett. **94**, 454–460 (1983).

[16] S. Leach, N. C. Jones, S. V. Hoffmann, and S. Un, "Isoquinoline gas-phase absorption spectrum in the vacuum ultraviolet between 3.7 and 10.7 eV. New valence and Rydberg electronic states," RSC Adv. **9**, 5121–5141 (2019).

[17] V. Krishnakumar and R. Ramasamy, "DFT studies and vibrational spectra of isoquinoline and 8-hydroxyquinoline," Spectrochim. Acta, Part A **61**, 673–683 (2005).

[18] K. K. Innes, I. G. Ross, and W. R. Moomaw, "Electronic states of azabenzenes and azanaphthalenes: A revised and extended critical review," J. Mol. Spectrosc. **132**, 492–544 (1988).

[19] J. Wanna and E. R. Bernstein, "van der Waals clusters of pyridazine and isoquinoline: The effect of solvation on chromophore electronic structure," J. Chem. Phys. **86**, 6707–6716 (1987).

[20] A. Hiraya, Y. Achiba, K. Kimura, and E. C. Lim, "Identification of the lowest energy $n\pi^*$ states in gas-phase polycyclic monoazines: Quinoline and isoquinoline," J. Chem. Phys. **81**, 3345–3347 (1984).

[21] A. Hiraya, Y. Achiba, K. Kimura, and E. C. Lim, "Multiphoton ionization photoelectron spectroscopy of molecular excited states in supersonic jet: Low-lying electronic states of isoquinoline," Chem. Phys. Lett. **185**, 303–309 (1991).

[22] K. H. Hassan and J. Hollas, "Rotational contour analysis of bands in the 313 nm electronic spectrum of isoquinoline: Evidence for $\pi\pi^*$ character and coriolis coupling," Chem. Phys. **129**, 477–482 (1989).

[23] Z. Kisiel, O. Desyatnyk, L. Pszczółkowski, S. Charnley, and P. Ehrenfreund, "Rotational spectra of quinoline and of isoquinoline: Spectroscopic constants and electric dipole moments," J. Mol. Spectrosc. **217**, 115–122 (2003).

[24] D. F. Plusquellic, R. Suenram, B. Mate, J. Jensen, and A. Samuels, "The conformational structures and dipole moments of ethyl sulfide in the gas phase," J. Chem. Phys. **115**, 3057–3067 (2001).

[25] D. F. Plusquellic, Jb64 spectra fitting program, see https://www.nist.gov/services-resources/software/jb95-spectral-fitting-program, Gaithersburg, Boulder, 2014.

[26] C. Brand, J. Küpper, D. W. Pratt, W. Leo Meerts, D. Krügler, J. Tatchen, and M. Schmitt, "Vibronic coupling in indole: I. Theoretical description of the ^1L_a–^1L_b interaction and the electronic spectrum," Phys. Chem. Chem. Phys. **12**, 4968–4979 (2010).

[27] J. Küpper, D. W. Pratt, W. Leo Meerts, C. Brand, J. Tatchen, and M. Schmitt, "Vibronic coupling in indole: II. investigation of the ^1L_a–^1L_b interaction using rotationally resolved electronic spectroscopy," Phys. Chem. Chem. Phys. **12**, 4980–4988 (2010).

[28] O. Christiansen, J. Gauss, J. F. Stanton, and P. Jørgensen, "The electronic spectrum of pyrrole," J. Chem. Phys. **111**, 525–537 (1999).

[29] C. M. Marian, "A new pathway for the rapid decay of electronically excited adenine," J. Chem. Phys. **122**, 104314 (2005).

[30] B. F. Parsons and D. E. Szpunar, "Investigation of O_2–X (X = pyrrole or pyridine) cluster photodissociation near 226 nm," J. Phys. Chem. A **124**, 10152–10161 (2020).

[31] B. F. Parsons, M. R. Rivera, and M. K. Onder, "NO (A) rotational state distributions from photodissociation of the N_2-NO complex," J. Phys. Chem. A **126**, 5729–5737 (2022).

[32] U. Even, J. Jortner, D. Noy, N. Lavie, and C. Cossart-Magos, "Cooling of large molecules below 1 K and He clusters formation," J. Chem. Phys. **112**, 8068–8071 (2000).

[33] U. Even, "The Even-Lavie valve as a source for high intensity supersonic beam," EPJ Tech. Instrum. **2**, 17–22 (2015).

[34] L. Minnhagen, "The energy levels of neutral atomic iodine," Arkiv Fysik **21**, 415–465 (1962).

[35] G. Li Manni, I. Fdez Galván, A. Alavi, F. Aleotti, F. Aquilante, J. Autschbach, D. Avagliano, A. Baiardi, J. J. Bao, S. Battaglia, L. Birnoschi, A. Blanco-González, S. I. Bokarev, R. Broer, R. Cacciari, P. B. Calio, R. K. Carlson, R. Carvalho Couto, L. Cerdán, L. F. Chibotaru, N. F. Chilton, J. R. Church, I. Conti, S. Coriani, J. Cuéllar-Zuquin, R. E. Daoud, N. Dattani, P. Decleva, C. de Graaf, M. G. Delcey, L. De Vico, W. Dobrautz, S. S. Dong, R. Feng, N. Ferré, M. Filatov(Gulak, L. Gagliardi, M. Garavelli, L. González, Y. Guan, M. Guo, M. R. Hennefarth, M. R. Hermes, C. E. Hoyer, M. Huix-Rotllant, V. K. Jaiswal, A. Kaiser, D. S. Kaliakin, M. Khamesian, D. S. King, V. Kochetov, M. Krośnicki, A. A. Kumaar, E. D. Larsson, S. Lehtola, M.-B. Lepetit, H. Lischka, P. López Ríos, M. Lundberg, D. Ma, S. Mai, P. Marquetand, I. C. D. Merritt, F. Montorsi, M. Mörchen, A. Nenov, V. H. A. Nguyen, Y. Nishimoto, M. S. Oakley, M. Olivucci, M. Oppel, D. Padula, R. Pandharkar, Q. M. Phung, F. Plasser, G. Raggi, E. Rebolini, M. Reiher, I. Rivalta, D. Roca-Sanjuán, T. Romig, A. A. Safari, A. Sánchez-Mansilla, A. M. Sand, I. Schapiro, T. R. Scott, J. Segarra-Martí, F. Segatta, D.-C. Sergentu, P. Sharma, R. Shepard, Y. Shu, J. K. Staab, T. P. Straatsma, L. K. Sørensen, B. N. C. Tenorio, D. G. Truhlar, L. Ungur, M. Vacher, V. Veryazov, T. A. Voß, O. Weser, D. Wu, X. Yang, D. Yarkony, C. Zhou, J. P. Zobel, and R. Lindh, "The OpenMolcas *Web*: A community-driven approach to advancing computational chemistry," J. Chem. Theory Comput. (published online 2023).

[36] K. Andersson, P. A. Malmqvist, B. O. Roos, A. J. Sadlej, and K. Wolinski, "Second-order perturbation theory with a CASSCF reference function," J. Phys. Chem. **94**, 5483–5488 (1990).

[37] K. Andersson, P. Malmqvist, and B. O. Roos, "Second-order perturbation theory with a complete active space self-consistent field reference function," J. Chem. Phys. **96**, 1218–1226 (1992).

[38] Y. Nishimoto, "Analytic gradients for restricted active space second-order perturbation theory (RASPT2)," J. Chem. Phys. **154**, 194103 (2021).

[39] Y. Nishimoto, S. Battaglia, and R. Lindh, "Analytic first-order derivatives of (X)MS, XDW, and RMS variants of the CASPT2 and RASPT2 methods," J. Chem. Theory Comput. **18**, 4269–4281 (2022).

[40] B. O. Roos, R. Lindh, P.-Å. Malmqvist, V. Veryazov, and P.-O. Widmark, "Main group atoms and dimers studied with a new relativistic ANO basis set," J. Phys. Chem. A **108**, 2851–2858 (2004).

[41] B. O. Roos, R. Lindh, P.-Å. Malmqvist, V. Veryazov, and P.-O. Widmark, "New relativistic ANO basis sets for transition metal atoms," J. Phys. Chem. A **109**, 6575–6579 (2005).

[42] L. Serrano-Andrés, M. Merchán, M. Fülscher, and B. O. Roos, "A theoretical study of the electronic spectrum of thiophene," Chem. Phys. Lett. **211**, 125–134 (1993).

[43] D. J. Tozer, R. D. Amos, N. C. Handy, B. O. Roos, and L. Serrano-ANDRES, "Does density functional theory contribute to the understanding of excited states of unsaturated organic compounds?," Mol. Phys. **97**, 859–868 (1999).

[44] C. Angeli, S. Borini, and R. Cimiraglia, "An application of second-order n-electron valence state perturbation theory to the calculation of excited states," Theor. Chem. Acc. **111**, 352–357 (2004).

[45] R. Sarkar, P.-F. Loos, M. Boggio-Pasqua, and D. Jacquemin, "Assessing the performances of CASPT2 and NEVPT2 for vertical excitation energies," J. Chem. Theory Comput. **18**, 2418–2436 (2022).

[46] T. B. Pedersen, F. Aquilante, and R. Lindh, "Density fitting with auxiliary basis sets from Cholesky decompositions," Theor. Chem. Acc. **124**, 1–10 (2009).

[47] W. A. de Jong, R. J. Harrison, and D. A. Dixon, "Parallel Douglas–Kroll energy and gradients in NWChem: Estimating scalar relativistic effects using Douglas–Kroll contracted basis sets," J. Chem. Phys. **114**, 48 (2001).

[48] C. Kollmar, K. Sivalingam, Y. Guo, and F. Neese, "An efficient implementation of the NEVPT2 and CASPT2 methods avoiding higher-order density matrices," J. Chem. Phys. **155**, 234104 (2021).

[49] F. Neese, "Prediction of molecular properties and molecular spectroscopy with density functional theory: From fundamental theory to exchange-coupling," Coord. Chem. Rev. **253**, 526–563 (2009).

[50] F. Neese, F. Wennmohs, U. Becker, and C. Riplinger, "The ORCA quantum chemistry program package," J. Chem. Phys. **152**, 224108 (2020).

[51] A. K. Dutta, F. Neese, and R. Izsák, "Speeding up equation of motion coupled cluster theory with the chain of spheres approximation," J. Chem. Phys. **144**, 034102 (2016).

[52] J. P. Perdew, K. Burke, and M. Ernzerhof, "Generalized gradient approximation made simple," Phys. Rev. Lett. **77**, 3865–3868 (1996).

[53] C. Adamo and V. Barone, "Toward reliable density functional methods without adjustable parameters: The PBE0 model," J. Chem. Phys. **110**, 6158–6170 (1999).

[54] A. D. Becke, "Density-functional exchange-energy approximation with correct asymptotic behavior," Phys. Rev. A **38**, 3098–3100 (1988).

[55] C. Lee, W. Yang, and R. G. Parr, "Development of the Colle-Salvetti correlation-energy formula into a functional of the electron density," Phys. Rev. B **37**, 785–789 (1988).

[56] S. H. Vosko, L. Wilk, and M. Nusair, "Accurate spin-dependent electron liquid correlation energies for local spin density calculations: A critical analysis," Can. J. Phys. **58**, 1200–1211 (1980).

[57] E. Runge and E. K. U. Gross, "Density-functional theory for time-dependent systems," Phys. Rev. Lett. **52**, 997–1000 (1984).

[58] T. H. Dunning, Jr., "Gaussian basis sets for use in correlated molecular calculations. I. The atoms boron through neon and hydrogen," J. Chem. Phys. **90**, 1007–1023 (1989).

[59] F. Weigend, "Accurate coulomb-fitting basis sets for H to Rn," Phys. Chem. Chem. Phys. **8**, 1057–1065 (2006).

[60] F. Weigend, A. Köhn, and C. Hättig, "Efficient use of the correlation consistent basis sets in resolution of the identity MP2 calculations," J. Chem. Phys. **116**, 3175–3183 (2002).

[61] C. Kollmar, K. Sivalingam, B. Helmich-Paris, C. Angeli, and F. Neese, "A perturbation-based super-CI approach for the orbital optimization of a CASSCF wave function," J. Comput. Chem. **40**, 1463–1470 (2019).

[62] S. C. Wait, Jr. and J. C. McNerney, "Vibrational spectra and assignments for quinoline and isoquinoline," J. Mol. Spectrosc. **34**, 56–77 (1970).

[63] C. Marian, D. Nolting, and R. Weinkauf, "The electronic spectrum of protonated adenine: Theory and experiment," Phys. Chem. Chem. Phys. **7**, 3306–3316 (2005).

[64] R. Weinkauf, L. Lehr, E. W. Schlag, S. Salzmann, and C. M. Marian, "Ultrafast dynamics in thiophene investigated by femtosecond pump probe photoelectron spectroscopy and theory," Phys. Chem. Chem. Phys. **10**, 393–404 (2008).

[65] J. Lee, D. W. Small, and M. Head-Gordon, "Excited states via coupled cluster theory without equation-of-motion methods: Seeking higher roots with application to doubly excited states and double core hole states," J. Chem. Phys. **151**, 214103 (2019).

[66] D. Jacquemin, I. Duchemin, and X. Blase, "Is the Bethe–Salpeter formalism accurate for excitation energies? Comparisons with TD-DFT, CASPT2, and EOM-CCSD," J. Phys. Chem. Lett. **8**, 1524–1529 (2017).